Hindawi Publishing Corporation
Journal of Nanomaterials
Volume 2013, Article ID 648346, 9 pages
http://dx.doi.org/10.1155/2013/648346

Research Article

Fabrication of Mo+N-Codoped TiO_2 Nanotube Arrays by Anodization and Sputtering for Visible Light-Induced Photoelectrochemical and Photocatalytic Properties

Min Zhang, Dandan Lu, Guotian Yan, Juan Wu, and Jianjun Yang

Key Laboratory for Special Functional Materials of Ministry of Education, Henan University, Kaifeng 475004, China

Correspondence should be addressed to Min Zhang; zm1012@henu.edu.cn and Jianjun Yang; yangjianjun@henu.edu.cn

Received 26 August 2013; Accepted 18 November 2013

Academic Editor: Shenmin Zhu

Mo,N-codoped TiO_2 nanotube arrays (TNAs) were fabricated by a two-step method consisting of electrochemical anodization and subsequent magnetron sputtering of Mo. The samples were characterized by scanning electron microscopy (SEM), X-ray diffraction (XRD), X-ray photoelectron spectroscopy (XPS), and ultraviolet-visible diffuse reflectance spectroscopy (UV-Vis DRS). The results showed that the Mo,N-codoped TiO_2 nanotube arrays exhibited higher visible light absorbance and remarkably enhanced photocurrent density and photocatalytic activity compared with single N-doped TiO_2. The highly efficient photoelectrochemical and photocatalytic activity is associated with the codoping effect between Mo and N, which plays a key role in producing new states, narrowing the bandgap, and reducing the recombination thereby effectively improving the visible light absorption and photocatalytic activity of TNAs.

1. Introduction

TiO_2 is one of the most studied compounds in materials science and widely used in the fields of photocatalysis, dye-sensitized solar cells, and biomedical devices owing to its outstanding chemical and physical properties, such as ease of synthesis, chemical stability, and long lifetime of electron/hole pairs [1]. Compared to other types of titania nanostructures, TiO_2 nanotube arrays (TNAs) have the advantage of high surface-to-volume ratios and size-dependent properties for applications in photocatalysis, sensing, and photovoltaics [2–4]. TNAs with different sizes and geometrical shapes have been prepared using various physical and chemical synthesis routes [5–7]. Among these fabrication techniques, electrochemical anodization is an efficient and economical approach for the production of highly ordered TNAs with controllable tube size and morphology [8–10]. Highly ordered TNAs exhibited excellent photocatalytic properties due to their high-oriented uniform nanotube architecture and the rapid transfer of the photogenerated holes to the surrounding electrolyte and the extended electron lifetimes in the nanotubes [11, 12].

Due to its large band gap (about 3.2 eV), TiO_2 fails to absorb a significant fraction of visible light effectively, resulting in a poor solar-to-hydrogen conversion efficiency. Doping, in particular the doping by N, has attracted increasing attention due to its effectiveness in realizing visible-light photocatalytic activity of TiO_2 [13, 14]. However, single doping of nitrogen also creates some problems such as low UV light photoactivity, unstable N species after photocatalysis, and low oxidation power of the photogenerated hole. For TiO_2 nanotube arrays, traditional solution-based N doping typically leads to XPS peaks above 400 eV, which can be interpreted as an interstitial doping or sensitization in many reports. Moreover, the N doping level is usually very low. This solution-based N doping sometimes compromises the effectiveness of band gap narrowing and provides numerous recombination centers resulting in the loss of photogenerated electron-hole pairs. Accordingly, the visible absorbance and the photoactivity of single N-doped TiO_2 are rather limited [2, 3, 15].

In order to improve the visible-light photocatalytic performance of N-doped TiO_2 catalysts, the modification of doping strategy has been extensively adopted by many

researchers. Nitrogen and various modification substances such as metal, metal oxide, and other nonmetal codoped TiO_2 catalysts have been widely investigated [16–19]. The modified N-doped TiO_2 usually showed favorable effects for improving the visible-light photocatalytic activity compared to single N-doped TiO_2. Moreover, some researchers reported that the presence of other dopants promoted more nitrogen atoms to be incorporated into the lattice of TiO_2. Gu et al. reported that the N concentration in V,N-codoped TiO_2 was higher than that in N–TiO_2 due to the distortion of the anatase lattice and charge compensation in the presence of V ions [20]. Wang et al. claimed that the introduction of ZrO_2 can effectively stabilize the nitrogen in the TiO_2 matrix. They found that N–Ti–O bond in the $ZrO_2/TiO_{2-x}N_x$ remained even after heating the $ZrO_2/TiO_{2-x}N_x$ sample at 600°C [21].

Recently, Mo and N-doped TiO_2 nanostructures have been synthesized with various methods to obtain enhanced visible-light photocatalytic activity. Tan et al. prepared Mo, N-codoped anatase nanocrystalline TiO_2 by a sol-gel method [22]. Recently, Zhang et al. found a hydrothermal route to obtain Mo+N-codoped TiO_2 nanosheets with dominant {001} facets [23]. To our knowledge, few studies have been reported about the fabrication of Mo,N-codoped TiO_2 nanotube arrays up to now. In the present work, we have fabricated Mo,N-codoped TNAs by magnetron sputtering of Mo on the electrochemically anodized TNAs. The photoelectrochemical and photocatalytic properties of codoped TNAs were investigated under visible light irradiation and compared with those of single N-doped TNAs.

2. Experimental Section

2.1. Preparation. Self-organized and well-aligned TNAs were fabricated by electrochemical anodization process. Briefly, commercial titanium sheets (20 mm × 40 mm, purity > 99.6%;) with a thickness of 0.25 mm were sequentially sonicated in acetone, isopropanol, and methanol for 10 min, followed by etching in the mixture of $HF/HNO_3/H_2O$ (1 : 4 : 5 in volume) for 20 s, rinsing with deionized water, and drying under a N_2 stream. Resultant rectangular Ti sheet was used as an anode to couple with Pt meshwork as a cathode in the anodic oxidation test setup. A direct current power supply and a mixed electrolyte solution of ethylene glycol containing 1 wt% NH_4F and 2 vol% deionized water were used in the electrochemical processes. The oxidation was conducted at 60 V for 3 h. Magnetic stirring was adopted throughout the oxidation processes while a circulation pump was performed at a low temperature of about 20°C. After anodization, all samples were sonicated in ethanol and dried under high purity N_2 stream to obtain the as-prepared TNAs.

Sputtering process was conducted to deposit Mo on the as-prepared TNAs using a DC magnetron sputtering (FDJ-600, Shenyang Vacuum Equipment Co., Ltd.) under the pressure 2.9×10^{-2} Pa. Then, the samples were calcined in air at 600°C for 3 h at a heating rate of 1°C/min in a tube furnace and naturally cooled to room temperature. Three types of samples are obtained by varying the time of Mo deposition, that is, 5 min, 30 min and, 60 min, and denoted as Mo-N-TiO_2-5, Mo-N-TiO_2-30, and Mo-N-TiO_2-60, respectively. For comparison, the as-prepared TNAs were also calcined in air at the same temperature and denoted as N-TiO_2.

2.2. Characterization. The morphologies of N-TiO_2 and Mo, N-codoped TNAs were characterized with a SEM, (JSM5600LV, Japan). A scanning UV-Vis spectrophotometer (Cary 5000, Varian, USA) equipped with a Labsphere diffuse reflectance accessory was used to collect the reflectance spectra of N-TiO_2 and Mo,N-codoped TNAs in the range of 250–700 nm at a scan speed of 300 nm min^{-1}. The Raman spectra were measured by a laser Raman spectrometer (Renishaw-1000) with a 457.5 nm solid-state laser. Chemical state analysis was carried out on an Axis Ultra XPS instrument (Kratos, UK) using a 210 W monochromatic Al source with a pass energy of 20 eV and a step of 0.1 eV. All XPS spectra were corrected using the C1s line at 284.8 eV.

2.3. Photoelectrochemical and Photocatalytic Activity Measurements. Photocurrents were measured by an electrochemical analyzer (IM6eX Instruments, ZAHNER, German) in a standard three-electrode system using the prepared samples as the working electrodes with an active area of ca. 4 cm^2. A Pt meshwork was used as the counter electrode and Ag/AgCl was used as a reference electrode. A 300 W Xenon lamp (PLS-SEX300, Beijing Changtuo) was used as the light source. A cut-off filter was used to remove any radiation below 420 nm to ensure visible light irradiation only. The light intensity was measured by a photodetector, and the value is about 30 mW/cm^2 at 420 nm. A 1 M KOH aqueous solution was used as the electrolyte.

Photocatalytic activity of all samples was evaluated by monitoring the photocatalytic degradation of methylene blue (MB) in aqueous solution under visible light with vertical irradiation as light source. Briefly, to-be-tested N-TiO_2 and Mo-N-TiO_2-X (X = 5, 30, and 60) samples were dipped into 25 mL of MB solution with an initial concentration of 10 mg L^{-1}. The effective photocatalytic reaction area of all samples was 4 cm^2. Prior to irradiation, the MB solution containing to-be-tested sample was magnetically stirred in the dark for 30 min to establish adsorption–desorption equilibrium. During the photocatalytic reaction, the absorbance of MB at 664 nm was measured using an SP-2000 spectrophotometer at a time interval of 30 min. The decoloration rate of MB solution is calculated as $(C_0 - C)/C_0 \times 100\%$, where C_0 is the concentration of MB at adsorption-desorption equilibrium in the dark and C is the concentration of MB upon completion of the photocatalytic reaction under visible light irradiation. In this way, the influence of adsorption amount of MB on its solution decoloration rate is excluded (different photocatalyst samples adsorb different amount of MB).

3. Results and Discussion

3.1. SEM Images. The morphologies of N-TiO_2 and Mo,N-codoped TNAs were observed by SEM. Figure 1(a) shows the typical top view and cross-sectional SEM images of N-TiO_2 nanotube arrays. Large-scale ordered nanotube arrays structures were found with the average diameter of ca.

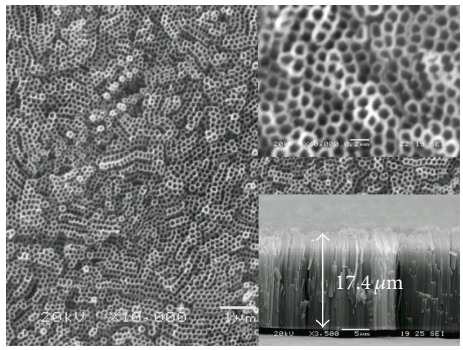

(a)

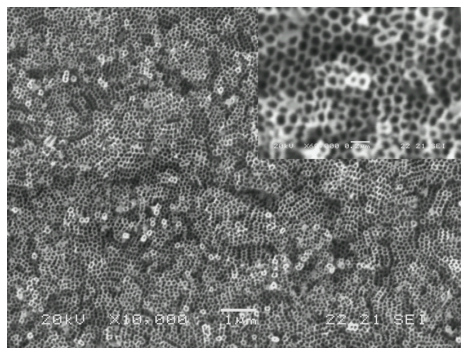

(b)

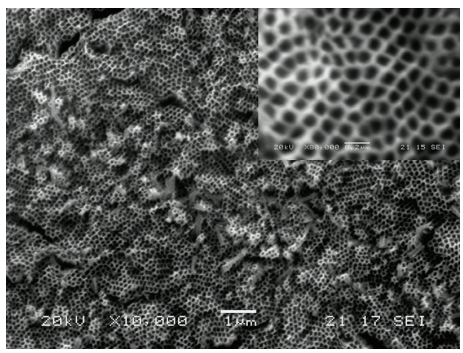

(c)

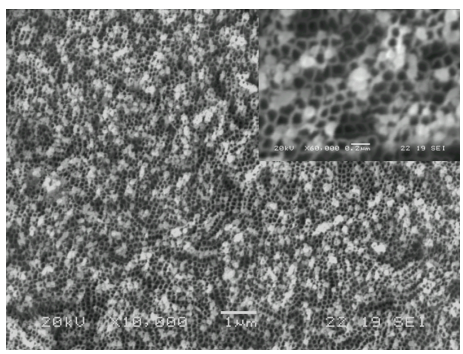

(d)

Figure 1: SEM images of the N-TiO_2 (a), Mo-N-TiO_2-5 (b), Mo-N-TiO_2-30 (c), and Mo-N-TiO_2-60 (d).

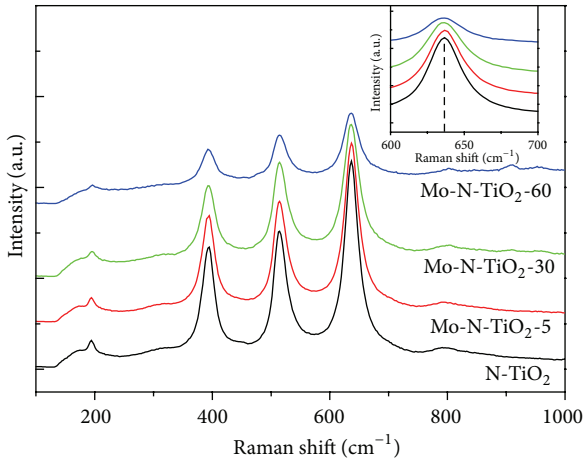

FIGURE 2: Raman spectra of N-TiO_2 and Mo,N-codoped TiO_2 nanotube arrays. Inset shows an expanded view for the peak of 637 cm^{-1} in the Raman spectra.

130 nm. The cross-sectional SEM observation in Figure 1(a) clearly shows that the N-TiO_2 nanotube arrays were well aligned and vertically oriented on the titanium substrate with a length of ca. 17.4 μm. Figures 1(b) and 1(c) present the morphologies of Mo,N-codoped TNAs samples with Mo deposition of 5 min and 30 min. No distinct deposit appeared on the surface of calcined TNAs with Mo deposition time less than 30 min. It indicates that the Mo doping is into the TNAs. SEM image (Figure 1(d)) of calcined TiO_2 nanotube arrays with Mo deposition time of 60 min shows clear difference from the previous images. It shows that the surface of Mo-N-TiO_2-60 sample is covered by a large number of particles. The SEM observations clearly show that an optimal Mo deposition duration is important to get useful Mo,N-codoped TNAs. The amount of doping would be not enough to get the visible-light response with a short deposition duration. However, the aggregates of Mo or Mo oxides deposition on the TNAs with long deposition time may block the nanotubes resulting in a poor photoelectrochemical performance.

3.2. Crystal Structure. Raman spectroscopy has been employed as a sensitive technique to examine phase composition and surface homogeneity. Figure 2 shows the Raman spectra of the single N-TiO_2 and Mo,N-codoped TNAs. Four typical Raman peaks at about 195, 393, 515, and 637 cm^{-1} for all samples are corresponding to the E_g, B_{1g}, A_{1g}, and E_g modes of the anatase phase of TiO_2, respectively. It indicates that the anatase phase dominates the crystal structure of all doped samples. However, the peak intensity of anatase TiO_2 is gradually decreased along with the increase of Mo content, which may be due to the fact that the formation of Mo–O–Ti bonds inhibited the crystallite growth of TiO_2 during calcination. Moreover, compared with N-TiO_2, the Raman peak of the Mo,N-codoped TiO_2 at ~637 cm^{-1} exhibits a slight shift to low wavenumber. The expanded pattern about the Raman peaks at ~637 cm^{-1} is represented in the inset of Figure 2. It is known that the ionic radius of Mo^{6+} (0.062 nm) is little smaller than that of Ti^{4+} (0.068 nm). As a result, lattice contraction occurs where Ti^{4+} is substituted with Mo^{6+} in the TiO_2 lattice due to the difference of the ionic radius, resulting in the increase of phonon frequency. Generally, blue shift of Raman band is simultaneous with the increase of phonon frequency in some crystalline phase [22]. Herein, the blueshift of Raman peaks at ~637 cm^{-1} can be ascribed to the increase of the phonon frequency due to Mo doping.

3.3. XPS Analyses. High-resolution XPS of N1s and Mo 3d core levels were measured to obtain-detailed chemical state information for N-TiO_2 and Mo,N-codoped TNAs. Figure 3(a) shows the high-resolution XPS spectra of the Mo 3d region for the Mo,N-codoped TiO_2 nanotube arrays. The assignment of oxidation states of different Mo oxides is based on the Mo (3d3/2, 3d5/2) spin-orbit components. These energies are at 235.85 and 232.65 eV for MoO_3, 234.9 and 231.7 eV for Mo_2O_5, 232.3, 229.1 eV for MoO_2, and 230.85 and 227.7 eV for Mo(0) [24, 25]. After deconvolution of Mo 3d peak, the binding energies of 232.6 and 235.8 eV are corresponding to Mo3d5/2 and Mo3d3/2 in MoO_3 for Mo,N-codoped TNAs, respectively. The 235.1 and 231.8 eV for Mo_2O_5 are also found for Mo-N-TiO_2-30 sample which hints the presence of Mo^{5+}. The presence of Mo^{5+} in the Mo-N-TiO_2-30 catalysts may be due to the reduction of Mo^{6+} by Ti^{3+} generated during the calcinations of the catalysts [26]. Since the ionic radius of six-coordinated Mo^{6+} (0. 062 nm) is very close to that of Ti^{4+} in TiO_2 (0. 068 nm), Mo^{6+} ions can easily substitute Ti^{4+} ions in TiO_2 lattice.

Figure 3(b) shows the XPS spectra for the N1s region and their fitting curves for N-TiO_2 and Mo,N-codoped TNAs. For the N-TiO_2 nanotube arrays, the binding energy at 400.3 eV of N1s can be interpreted as an interstitial doping or sensitization. Varghese et al. reported that the nitrogen incorporated within the nanotubes during anodization was primarily supplied by the NH_4F [15]. However, the annealing process of single nitrogen-incorporated samples at high temperatures in an oxygen-rich environment generally may remove the doped nitrogen by oxidation and lead to inefficacy of bandgap narrowing. For all the fitting curves of Mo,N-codoped TNAs shown in Figure 3(b), the deconvolution of N 1s peak revealed the presence of two peaks with binding energy at 399.8 and 398.6 eV. The N 1s peak localized at 398.6 eV can be ascribed to anionic N incorporated in TiO_2 in O–Ti–N linkages, while the peak at 399.8 eV can be attributed to the presence of oxidized nitrogen such as N–O–Ti from the previous reports [13, 27, 28]. Therefore, the XPS results indicated that two forms of O–Ti–N and N–O–Ti coexist in Mo,N-codoped TNAs.

Figure 3(c) presents high-resolution Ti 2p XPS spectra of all samples. For N-TiO_2 sample, two peaks at 458.4 and 464.1 eV correspond to the Ti 2p3/2 and Ti 2p1/2 states, indicating that Ti is 4+ valence. For the Mo,N-codoped TiO_2 sample, Ti 2p peaks are slightly shifted toward higher binding energy due to the doping of Mo in the TiO_2 lattice and the formation of neighboring oxygen vacancies showing a high electron-attracting effect [29, 30]. Moreover, the Ti 2p3/2 peak of Mo-N-TiO_2-30 sample became remarkably

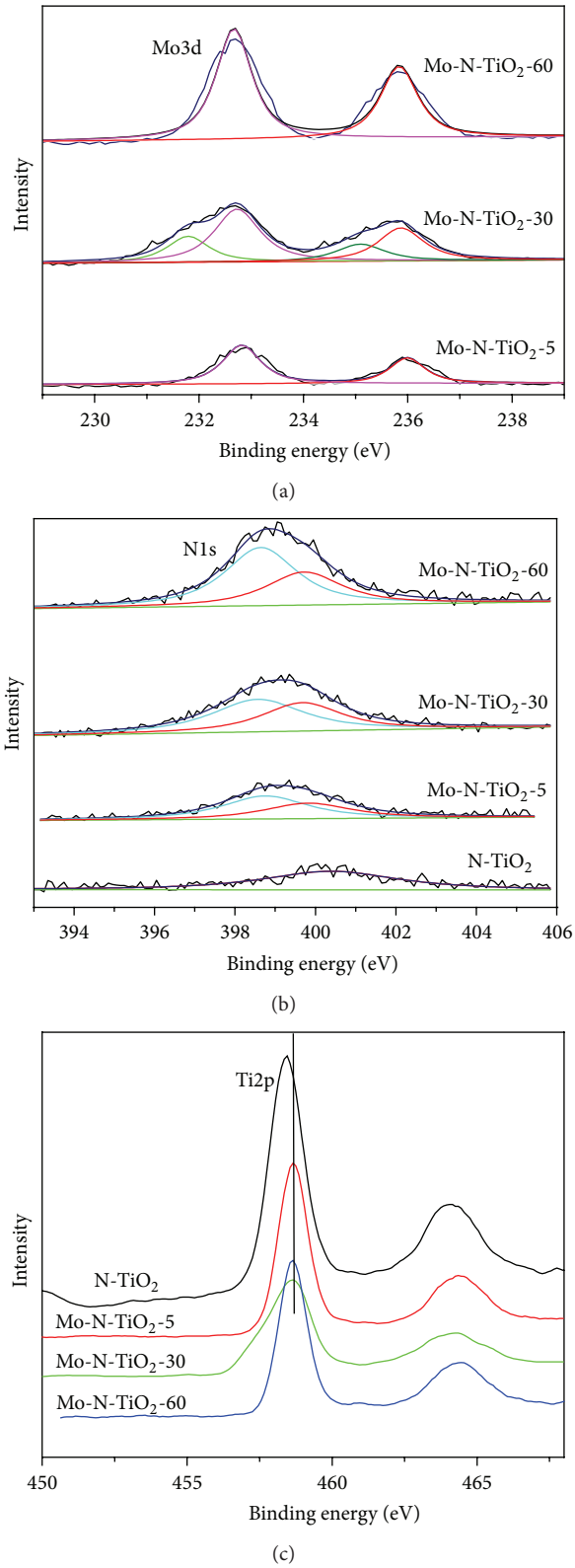

Figure 3: Peak-fitting XPS spectrum of Mo3d (a), N1s (b), and Ti2p (c) for N-TiO_2 and Mo,N-codoped TiO_2 nanotube arrays.

Table 1: Atomic concentration of surface of N-TiO_2 and Mo,N-codoped TiO_2 nanotube arrays.

Atomic concentration (at.%)	Sample			
	N-TiO_2	Mo-N-TiO_2-5	Mo-N-TiO_2-30	Mo-N-TiO_2-60
Ti	29.01	27.44	23.19	22.58
O	69.22	65.17	64.97	60.43
N	1.77	6.00	8.88	13.29
Mo	—	1.39	2.95	3.70

unsymmetrical compared with the peak of N-TiO_2 sample, indicating the existence of Ti^{3+} [31]. This result confirms that the Ti^{4+} can be reduced to Ti^{3+} during the calcinations of codoped samples when the dopant concentration is optimal. At the same time, Ti^{3+} species can reduce Mo^{6+} to Mo^{5+} when Mo was doped into the lattice of TiO_2. Some works also demonstrated that visible-light responsive TiO_2 can be fabricated by introducing Ti^{3+} accompanied by high vacancy concentration due to the formation of oxygen vacancy states with energies of 0.75–1.18 eV below the conduction band [30, 32].

The composition of all samples was also investigated and listed in Table 1. The N-TiO_2 sample shows a very low N doping level with a nitrogen concentration of about 1.77 atom percent (atom %) estimated from XPS analysis. For Mo,N-codoped TiO_2 nanotube arrays samples, the atomic concentration of nitrogen increased remarkably with the prolonging of Mo deposition time compared to that of the single N-TiO_2 sample. It indicated that more surface nitrogen incorporated in the lattice of TiO_2 can be promoted by Mo doping. The above XPS results show that the substitutional nitrogen atoms are present in addition to the interstitial nitrogen dopant after Mo was introduced into the lattice of TiO_2. In the meantime, the presence of Mo dopants allows more nitrogen atoms to be incorporated into the lattice of TiO_2, which show that the co-doping is in favor of enhancing the dopant solubility. Mo ions in the TiO_2 lattice may influence the incorporation of N into the lattice in two ways. Firstly, the existence of Mo ions brings about more distortion of the anatase lattice facilitating the incorporation of N into the lattice. Secondly, Mo ions further decrease the income resistance of N by the charge neutrality effect. This enhanced Mo and N co-doping effect observed in XPS results is very important for the bandgap narrowing of TiO_2 nanotube arrays and resulting visible light absorption.

3.4. UV-Vis DRS Spectra Analysis. The UV-Vis diffuse reflectance spectra of the single N- and Mo,N-codoped TiO_2 nanotube arrays are displayed in Figure 4. The spectrum obtained from the N-TiO_2 shows that N-TiO_2 primarily absorbs the ultraviolet light with a wavelength below 400 nm, which corresponds to the typical reported absorption feature of nitrogen-doped TiO_2 arising from the electron transition from surface state of NO_x species to the conduction band of TiO_2. We considered that the lower visible light absorption could be attributed to the low level of nitrogen doping, which was confirmed by XPS analysis. For the Mo,N-codoped TNAs sample of Mo-N-TiO_2-5, the UV-Vis DRS spectrum shows

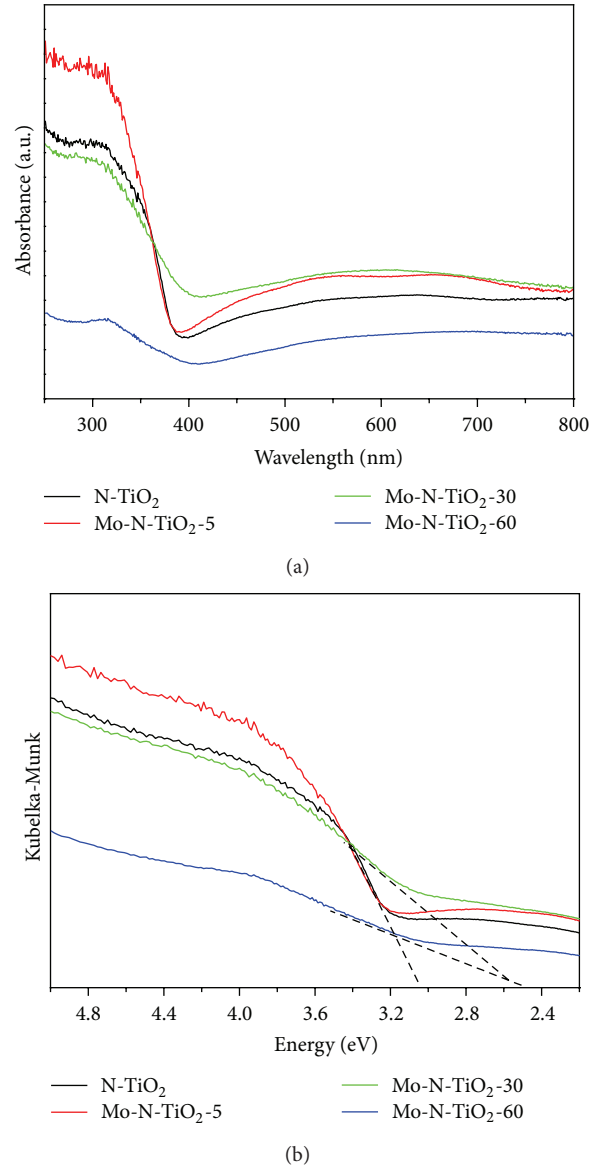

Figure 4: UV-Vis diffuse reflectance spectra of N-TiO_2 and Mo,N-codoped TiO_2 nanotube arrays.

a small red shift of the adsorption edge and a higher visible light absorbance. With the increase of Mo deposition time to 30 min, the doping of Mo and the existence of Ti^{3+} species led to a red shift of the absorption edge and caused significant absorbance in the visible-light region for Mo-N-TiO_2-30. For the Mo-N-TiO_2-60 sample, an obvious red shift of

the absorption edge was observed. Moreover, the intensities of the UV and visible light absorbance decreased remarkably due to the formation of a large number of Mo oxide particles covered on the surface of TNAs.

Kubelka-Munk function was used to estimate the band gap energy of the prepared samples by plotting $(\alpha hv)^{1/2}$ versus energy of absorbed light. The calculated results in Figure 4(b) indicated that the band gaps for N-TiO_2, Mo-N-TiO_2-5, Mo-N-TiO_2-30, and Mo-N-TiO_2-60 are 3.0, 3.0, 2.5, and 2.5 eV, respectively. It shows that the Mo,N-codoped TiO_2 nanotube array samples of Mo-N-TiO_2-30 and Mo-N-TiO_2-60 have a narrower band gap than that of N-TiO_2. When the dopant is in an optimal doping concentration, Mo^{6+} can easily substitute Ti^{4+} in the TiO_2 lattice, which might produce the new energy level and extend the light adsorption of TiO_2, due to the fact that ionic radius of Mo^{6+} (0.062 nm) is compatible with that of Ti^{4+} (0.068 nm). However, with a large amount of Mo doping, abundance of Mo^{6+} cannot dope into the lattice of TiO_2 and bring about the excessive aggregation of Mo oxide on the surface of TNAs and less influence on the adsorption edge.

3.5. Photoelectrochemical Properties. Photoelectrochemical method is usually applied to investigate the behavior of the transfer carriers within the photocatalysts and it provides useful information of the photocatalytic process. The photocurrent response measurements were carried out under visible light irradiation to investigate the photo-induced charges separation efficiency of N-TiO_2 and Mo,N-codoped TNAs samples. The transient photocurrents were measured at a fixed bias potential of 0.2 V versus SCE with a visible light pulse of 50 s. As can be seen from Figure 5, photocurrent values of all measured samples rapidly decrease to zero as soon as the irradiation of light turns off, and the photocurrents come back to a constant value when the light is again on with a good reproducibility. The results indicate that most of the photogenerated electrons under visible light irradiation are transported to the walls of TiO_2 nanotubes and then transferred to the titanium substrate to produce photocurrent.

It can be seen that the codoping has great effects on the density of photocurrent for TNAs. N-TiO_2 electrode shows only a lower photocurrent density of 4 $\mu A/cm^2$ due to its weak visible light absorbance. With the codoping of Mo and N, the photocurrent densities of Mo-N-TiO_2-5, Mo-N-TiO_2-30, and Mo-N-TiO_2-60 increase to 14 $\mu A/cm^2$, 19 $\mu A/cm^2$, and 5.8 $\mu A/cm^2$, respectively. For Mo-N-TiO_2-5, visible light absorbance increases remarkably compared to that of N-TiO_2 due to a small amount Mo doping, which results in the enhanced photocurrent response. Mo-N-TiO_2-30 sample had the highest photocurrent density due to the optimal Mo doping concentration resulting in the highest visible light absorbance. When the concentration of Mo is too high, the formation of MoO_3 aggregates may block the light absorbance of TiO_2 sample of Mo-N-TiO_2-60. The recombination center may also induce a decrease of photocurrent of Mo-N-TiO_2-60. Higher photocurrent means that more photoinduced electrons illuminated by visible light can transfer from TNAs to counter electrode via the external circuit efficiently. Photocatalytic activity of TiO_2 greatly depended on the electronhole transfer ability. Thus, it can be forecasted that the Mo,N-codoped TNAs would show higher visible-light photocatalytic activity than N-TiO_2.

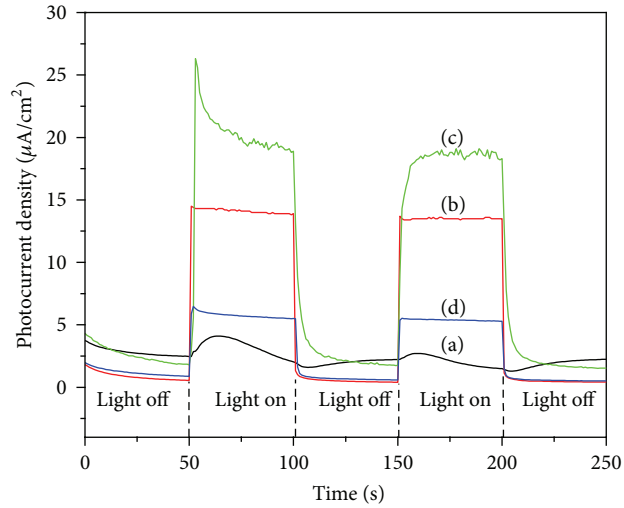

Figure 5: Transient photocurrents generated under pulse visible light irradiation at a fixed bias potential of 0.2 V (SCE) in a 1 M KOH solution for N-TiO_2 (a), Mo-N-TiO_2-5 (b), Mo-N-TiO_2-30 (c), and Mo-N-TiO_2-60 (d).

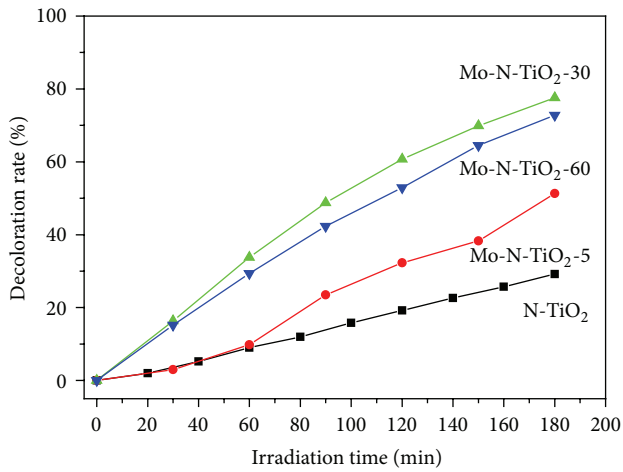

Figure 6: Photocatalytic degradation rate of MB in the presence of N-TiO_2 and Mo,N-codoped TiO_2 nanotube arrays under visible light irradiation.

3.6. Photocatalytic Activity. Photocatalytic activity of all doped TNAs samples was evaluated by monitoring the degradation of MB under visible light irradiation. As shown in Figure 6, Mo,N-codoped TNAs possess much higher photocatalytic activity under visible light irradiation than N-TiO_2. Besides, the decoloration rate of MB under visible light irradiation in the presence of Mo,N-codoped TNAs increases with the increase of dopant concentration. In particular, sample of Mo-N-TiO_2-30 exhibits the highest photocatalytic

activity among all the samples for the degradation of MB. It allows nearly 80% elimination of MB within 3 h.

The origin of the visible light photocatalytic activity of Mo,N-codoped TNAs can be attributed to the interactions between N doping and Mo doping. Before co-doping, interstitial N doping can induce the local states near the valence band edge and narrow the bandgap, which results in the visible-light photocatalytic activity of N-TiO_2 sample. After co-doping with Mo and N, Mo substitutes for Ti in the lattice and exists in the form of Mo^{6+}. The doping energy level of Mo^{6+}/Mo^{5+} is 0.4 eV, and it is much more positive than the potential of the conduction band of TiO_2 particles [E_{cb} = −0.5 eV versus NHE (normal hydrogen electrode) at pH = 1] [33, 34]. As a result, substitutional N atoms and interstitial N dopant coexist in the lattice after Mo incorporation. Moreover, Mo dopant allows more N atoms to be incorporated into the lattice of TiO_2. In this way, N 2*p* accepter state functions to narrow the bandgap of TiO_2 via mixing with O 2*p* states [13], while N is doped into the substitutive sites of TiO_2 during Mo,N-codoping. Consequently, bandgap energy of TiO_2 is significantly lowered and its absorption in the visible-light region is considerably increased. Mo,N-codoping makes it feasible for Mo,N-codoped TNAs to be activated by visible light, while more electrons and holes are generated to participate in photocatalytic reactions.

Moreover, the dopant concentration plays an important role in increasing photocatalytic activity of Mo,N-codoped TNAs in visible light region. Even a small amount of Mo^{6+} can act as a temporary photogenerated electron or hole-trapping site thereby inhibiting the recombination of photogenerated charge carriers and prolonging their lifetime [35, 36]. The detailed reaction steps are as follows:

$$\begin{aligned} TiO_2 + h\nu &\longrightarrow e^- + h^+ \\ Mo^{6+} + e^- &\longrightarrow Mo^{5+} \\ Mo^{5+} + O_2 &\longrightarrow Mo^{6+} + O_2{}^{-\bullet} \\ Mo^{6+} + h^+ &\longrightarrow Mo^{7+} \\ Mo^{7+} + OH^- &\longrightarrow Mo^{6+} + OH^\bullet \end{aligned} \quad (1)$$

When Mo^{6+} (d^5) trap an electron, its electronic configuration is transferred to d^6, and if it traps a hole, its electronic configuration will be transferred to d^4 which is highly unstable. Therefore, to restore the stable electronic configuration, the trapped charge carrier tends to be transferred from Mo^{5+} or Mo^{7+} to the adsorbed O_2 or surface hydroxyl (OH^-) thereby regenerating Mo^{6+}. These newly produced active species (such as $OH^\bullet$ and $O_2{}^{-\bullet}$) are able to initiate the photocatalytic reactions.

4. Conclusions

In summary, Mo,N-codoped TNAs showing visible light response were fabricated by a two-step method consisting of electrochemical anodization and subsequent sputter deposition. XPS results indicated the substitutional nitrogen atoms are present in addition to the interstitial nitrogen dopant after Mo doping into the lattice of TiO_2. Furthermore, the presence of Mo dopant allows more nitrogen atoms to be incorporated into the lattice of TiO_2. This enhanced co-doping effect is responsive for the bandgap narrowing of TNAs and subsequent visible-light adsorption. The results exhibited that the dopant concentration of TiO_2 nanotube arrays was an important parameter for photoelectrochemical and photoelectrocatalytic activities under visible light irradiation. When the Mo-doping time reached 30 min, the photocatalyst of Mo-N-TiO_2-30 showed the remarkably enhanced photocurrent density and highest photocatalyst activity. This work developed a simple approach to prepare codoped anatase TNAs and also gave a detailed discussion of co-doping mechanism of TNAs.

Acknowledgments

The authors thank the National Natural Science Foundation of China (no. 209730541 and no. 21203054) and Program for Changjiang Scholars and Innovation Research Team in University (no. PCS IRT1126).

References

[1] A. Fujishima, X. T. Zhang, and D. A. Tryk, "TiO_2 photocatalysis and related surface phenomena," *Surface Science Reports*, vol. 63, no. 12, pp. 515–582, 2008.

[2] Y.-C. Nah, I. Paramasivam, and P. Schmuki, "Doped TiO_2 and TiO_2 nanotubes: synthesis and applications," *ChemPhysChem*, vol. 11, no. 13, pp. 2698–2713, 2010.

[3] P. Roy, S. Berger, and P. Schmuki, "TiO_2 nanotubes: synthesis and applications," *Angewandte Chemie—International Edition*, vol. 50, no. 13, pp. 2904–2939, 2011.

[4] G. K. Mor, O. K. Varghese, M. Paulose, K. Shankar, and C. A. Grimes, "A review on highly ordered, vertically oriented TiO_2 nanotube arrays: fabrication, material properties, and solar energy applications," *Solar Energy Materials and Solar Cells*, vol. 90, no. 14, pp. 2011–2075, 2006.

[5] T. Kasuga, M. Hiramatsu, A. Hoson, T. Sekino, and K. Niihara, "Formation of titanium oxide nanotube," *Langmuir*, vol. 14, no. 12, pp. 3160–3163, 1998.

[6] J. H. Jung, H. Kobayashi, K. J. C. van Bommel, S. Shinkai, and T. Shimizu, "Creation of novel helical ribbon and double-layered nanotube TiO_2 structures using an organogel template," *Chemistry of Materials*, vol. 14, no. 4, pp. 1445–1447, 2002.

[7] Y. Zhu, H. Li, Y. Koltypin, Y. R. Hacohen, and A. Gedanken, "Sonochemical synthesis of titania whiskers and nanotubes," *Chemical Communications*, no. 24, pp. 2616–2617, 2001.

[8] A. Ghicov and P. Schmuki, "Self-ordering electrochemistry: a review on growth and functionality of TiO_2 nanotubes and other self-aligned MO_x structures," *Chemical Communications*, no. 20, pp. 2791–2808, 2009.

[9] P. Roy, D. Kim, K. Lee, E. Spiecker, and P. Schmuki, "TiO_2 nanotubes and their application in dye-sensitized solar cells," *Nanoscale*, vol. 2, no. 1, pp. 45–59, 2010.

[10] K. Lee, D. Kim, P. Roy et al., "Anodic formation of thick anatase TiO_2 mesosponge layers for high-efficiency photocatalysis," *Journal of the American Chemical Society*, vol. 132, no. 5, pp. 1478–1479, 2010.

[11] J. Y. Li, N. Lu, X. Quan, S. Chen, and H. M. Zhao, "Facile method for fabricating boron-doped TiO_2 nanotube array with enhanced photoelectrocatalytic properties," *Industrial and Engineering Chemistry Research*, vol. 47, no. 11, pp. 3804–3808, 2008.

[12] J. R. Jennings, A. Ghicov, L. M. Peter, P. Schmuki, and A. B. Walker, "Dye-sensitized solar cells based on oriented TiO_2 nanotube arrays: transport, trapping, and transfer of electrons," *Journal of the American Chemical Society*, vol. 130, no. 40, pp. 13364–13372, 2008.

[13] R. Asahi, T. Morikawa, T. Ohwaki, K. Aoki, and Y. Taga, "Visible-light photocatalysis in nitrogen-doped titanium oxides," *Science*, vol. 293, no. 5528, pp. 269–271, 2001.

[14] Y. Wang, C. X. Feng, M. Zhang, J. J. Yang, and Z. J. Zhang, "Visible light active N-doped TiO_2 prepared from different precursors: origin of the visible light absorption and photoactivity," *Applied Catalysis B*, vol. 104, pp. 268–274, 2011.

[15] O. K. Varghese, M. Paulose, T. J. LaTempa, and C. A. Grimes, "High-rate solar photocatalytic conversion of CO_2 and water vapor to hydrocarbon fuels," *Nano Letters*, vol. 9, no. 2, pp. 731–737, 2009.

[16] A. Kubacka, B. B. Baeza, G. Colon, and M. F. Garcia, "Doping level effect on sunlight-driven W,N-co-doped TiO_2-anatase photo-catalysts for aromatic hydrocarbon partial oxidation," *Applied Catalysis B*, vol. 93, no. 3-4, pp. 274–281, 2010.

[17] J. Choi, H. Park, and M. R. Hoffmann, "Effects of single metal-Ion doping on the visible-light photoreactivity of TiO_2," *Journal of Physical Chemistry C*, vol. 114, pp. 783–792, 2010.

[18] A. Kubacka, G. Colón, and M. Fernández-García, "N- and/or W-(co)doped TiO_2-anatase catalysts: effect of the calcination treatment on photoactivity," *Applied Catalysis B*, vol. 95, no. 3-4, pp. 238–244, 2010.

[19] G. T. Yan, M. Zhang, J. Hou, and J. J. Yang, "Photoelectrochemical and photocatalytic properties of N + S co-doped TiO_2 nanotube array films under visible light irradiation," *Materials Chemistry and Physics*, vol. 129, no. 1-2, pp. 553–557, 2011.

[20] D. E. Gu, B. C. Yang, and Y. D. Hu, "V and N co-doped nanocrystal anatase TiO_2 photocatalysts with enhanced photocatalytic activity under visible light irradiation," *Catalysis Communications*, vol. 9, no. 6, pp. 1472–1476, 2008.

[21] X. C. Wang, J. C. Yu, Y. L. Chen, L. Wu, and X. Z. Fu, "ZrO_2-modified mesoporous nanocrystalline $TiO_{2-x}N_x$ as efficient visible light photocatalysts," *Environmental Science and Technology*, vol. 40, no. 7, pp. 2369–2374, 2006.

[22] K. Q. Tan, H. R. Zhang, C. F. Xie, H. W. Zheng, Y. Z. Gu, and W. F. Zhang, "Visible-light absorption and photocatalytic activity in molybdenum- and nitrogen-codoped TiO_2," *Catalysis Communications*, vol. 11, no. 5, pp. 331–335, 2010.

[23] J. Zhang, J. H. Xi, and Z. G. Ji, "Mo + N codoped TiO_2 sheets with dominant {001} facets for enhancing visible-light photocatalytic activity," *Journal of Materials Chemistry*, vol. 22, pp. 17700–17708, 2012.

[24] S. H. Elder, F. M. Cot, Y. Su et al., "The discovery and study of nanocrystalline TiO_2-(MoO_3) core-shelf materials," *Journal of the American Chemical Society*, vol. 122, no. 21, pp. 5138–5146, 2000.

[25] H. Al-Kandari, F. Al-Kharafi, and A. Katrib, "Isomerization reactions of n-hexane on partially reduced MoO_3/TiO_2," *Catalysis Communications*, vol. 9, no. 5, pp. 847–852, 2008.

[26] S. Klosek and D. Raftery, "Visible light driven V-doped TiO_2 photocatalyst and its photooxidation of ethanol," *Journal of Physical Chemistry B*, vol. 105, no. 14, pp. 2815–2819, 2001.

[27] J. Wang, D. N. Tafen, J. P. Lewis et al., "Origin of photocatalytic activity of nitrogen-doped TiO_2 nanobelts," *Journal of the American Chemical Society*, vol. 131, no. 34, pp. 12290–12297, 2009.

[28] T. C. Jagadale, S. P. Takale, R. S. Sonawane et al., "N-doped TiO_2 nanoparticle based visible light photocatalyst by modified peroxide sol-gel method," *Journal of Physical Chemistry C*, vol. 112, no. 37, pp. 14595–14602, 2008.

[29] J. Y. Gong, W. H. Pu, C. Z. Yang, and J. L. Zhang, "Novel one-step preparation of tungsten loaded TiO_2 nanotube arrays with enhanced photoelectrocatalytic activity for pollutant degradation and hydrogen production," *Catalysis Communications*, vol. 36, pp. 89–93, 2013.

[30] M. Xing, J. Zhang, F. Chen, and B. Tian, "An economic method to prepare vacuum activated photocatalysts with high photoactivities and photosensitivities," *Chemical Communications*, vol. 47, no. 17, pp. 4947–4949, 2011.

[31] S. Hashimoto and A. Tanaka, "Alteration of Ti 2p XPS spectrum for titanium oxide by low-energy Ar ion bombardment," *Surface and Interface Analysis*, vol. 34, no. 1, pp. 262–265, 2002.

[32] D. C. Cronemeyer, "Infrared absorption of reduced rutile TiO_2 single crystals," *Physical Review*, vol. 113, no. 5, pp. 1222–1226, 1959.

[33] Z. Xu and J. Yu, "Visible-light-induced photoelectrochemical behaviors of Fe-modified TiO_2 nanotube arrays," *Nanoscale*, vol. 3, no. 8, pp. 3138–3144, 2011.

[34] Y. F. Li, D. H. Xu, J. Oh, W. Z. Shen, X. Li, and Y. Yu, "Mechanistic study of codoped titania with nonmetal and metal ions: a case of C + Mo codoped TiO_2," *ACS Catalysis*, vol. 2, pp. 391–398, 2012.

[35] L. G. Devi, S. G. Kumar, B. N. Murthy, and N. Kottam, "Influence of Mn^{2+} and Mo^{6+} dopants on the phase transformations of TiO_2 lattice and its photo catalytic activity under solar illumination," *Catalysis Communications*, vol. 10, no. 6, pp. 794–798, 2009.

[36] J. G. Yu, Q. J. Xiang, and M. H. Zhou, "Preparation, characterization and visible-light-driven photocatalytic activity of Fe-doped titania nanorods and first-principles study for electronic structures," *Applied Catalysis B*, vol. 90, pp. 595–602, 2009.